

RECEIVED: May 11, 2021
 REVISED: September 29, 2021
 ACCEPTED: October 4, 2021
 PUBLISHED: October 28, 2021

Fermion singlet dark matter in a pseudoscalar dark matter portal

Bastián Díaz Sáez,^a Patricio Escalona,^b Sebastián Norero^c and Alfonso Zerwekh^{d,e}

^a*Physik-Department, Technische Universität München,
 James-Frank-Straße, 85748 Garching, Germany*

^b*Departamento de Física, Universidad Técnica Federico Santa María,
 Avenida España 1680, Valparaíso, Chile*

^c*Instituto de Física, Pontificia Universidad Católica de Chile,
 Avenida Vicuña Mackenna 4860, Santiago, Chile*

^d*Departamento de Física y Centro Científico-Tecnológico de Valparaíso,
 Universidad Técnica Federico Santa María,
 Avenida España 1680, Valparaíso, Chile*

^e*Millennium Institute for Subatomic Physics at High Energy Frontier – SAPHIR,
 Fernandez Concha 700, Santiago, Chile*

E-mail: bastian.diaz@tum.de, patricio.escalona@sansano.usm.cl,
sebastian.norero@puc.cl, alfonso.zerwekh@usm.cl

ABSTRACT: We explore a simple extension to the Standard Model containing two gauge singlets: a Dirac fermion and a real pseudoscalar. In some regions of the parameter space both singlets are stable without the necessity of additional symmetries, then becoming a possible two-component dark matter model. We study the relic abundance production via freeze-out, with the latter determined by annihilations, conversions and semi-annihilations. Experimental constraints from invisible Higgs decay, dark matter relic abundance and direct/indirect detection are studied. We found three viable regions of the parameter space, and the model is sensitive to indirect searches.

KEYWORDS: Beyond Standard Model, Cosmology of Theories beyond the SM

ARXIV EPRINT: [2105.04255](https://arxiv.org/abs/2105.04255)

Contents

1	Introduction	1
2	The model	2
3	Relic density	4
3.1	Parameter space	4
3.2	Boltzmann equation	5
3.2.1	$m_s < m_h$	7
3.2.2	$m_s > m_h$	8
4	Phenomenology	9
4.1	Experimental constraints	10
4.2	Scan	10
4.3	Indirect detection	12
4.3.1	Box-shape gamma ray	13
4.3.2	Upper bounds	15
5	Discussion and conclusions	17
A	Annihilation cross sections	18

1 Introduction

Astrophysical evidence of dark matter (DM) has been accumulating for more than forty years now, but its fundamental nature remains unknown. From the particle physics points of view, different approaches have been carried out over the years to account for the elusive DM (for a review see [1]), and in particular, simple extensions to the SM containing gauge singlets look appealing for their simplicity, DM predictions and testable phenomenology [2–8]. Nowadays, those WIMP minimal extensions have been very constrained, especially by direct detection, motivating other possible alternatives. For instance, the interplay of a (pseudo)scalar and a fermion, both gauge singlets, open up the possibilities in many aspects: multi-component DM, new interaction channels, novel experimental signatures, small-scale structures, among others [9–29].

Keeping minimality, in this work we study a gauge singlet sector composed of a real pseudoscalar and a Dirac fermion. Depending on the coupling values and mass hierarchy between the singlets, the model admits a variety of DM productions with either one or the two singlets being stable. Two new interactions are present in the model: a Higgs portal and a dark sector coupling. The Higgs interaction is key because it regulates to what extent the dark sector is coupled to the SM, whereas the internal dark sector coupling only regulates

the coupling between the two singlets. In our knowledge, we study for the first time the WIMP regime of this framework in which both couplings take sizable values such that both singlets were in thermal equilibrium with the SM bath in the early universe. Interestingly, in certain mass hierarchy between the two singlets, the stability of both fields is guaranteed by a parity symmetry without the necessity of introducing new ad hoc discrete symmetries. Models with this last feature or accidental symmetries have been studied in different DM context, such as *Minimal Dark Matter* [30], spontaneous symmetry breaking [31], two DM components [32], vector DM [33, 34] and rank-two fields [35].

In the model under consideration, the DM relic abundance is triggered by annihilations, DM conversions [36] and semi-annihilations [37, 38], showing remarkable features in some regions of the parameter space. Further, we constraint the model considering the measured relic abundance in the universe, Higgs invisible decay and direct/indirect detection. For the latter, we explore box-shaped gamma ray spectra [39, 40], and we confront the available parameter space with Fermi-LAT data, CTA projections and AMS-02 bounds.

The paper is organized as follows. In section 2 we present the model and its theoretical constraints. In section 3 we explore the possible DM relic abundance mechanisms presents in the model, with a precise analysis of the two-component freeze-out scenario. In section 4 we review experimental constraints and the available parameter space along with indirect detection signals. In the last section we discuss and state our conclusions.

2 The model

The model adds to the SM two gauge singlets: one Dirac fermion ψ and a pseudo-scalar s . Under a parity transformation, the fields transform as $\psi \rightarrow \gamma^0 \psi$ and $s \rightarrow -s$, giving rise to the following Lagrangian:

$$\mathcal{L} = \mathcal{L}_{\text{SM}} + \bar{\psi}(i\not{\partial} - m_\psi)\psi + \frac{1}{2}(\partial_\mu s)^2 + ig_\psi s \bar{\psi} \gamma_5 \psi - V(H, s), \quad (2.1)$$

where the scalar potential is given by

$$V(H, s) = \mu^2 |H|^2 + \lambda_H |H|^4 + \frac{\mu_s^2}{2} s^2 + \frac{\lambda_s}{4!} s^4 + \frac{\lambda_{hs}}{2} |H|^2 s^2, \quad (2.2)$$

with H being the Higgs doublet.¹ We make g_ψ real under a fermion field redefinition such that the theory is CP-conserving. We assume that the singlet scalar does not acquire vacuum expectation value (vev), and after EWSB in the unitary gauge, $H = (0, (v_H + h)/\sqrt{2})^T$ with $v_H = 246$ GeV the Higgs vev, the scalar potential may be rewritten as

$$V(h, s) = \frac{\mu_s^2}{2} s^2 + \frac{\lambda_s}{4!} s^4 + \frac{\lambda_{hs}}{4} (h^2 + 2v_H h) s^2, \quad (2.3)$$

¹One may consider ψ as a sterile neutrino that mixes with the active ones. If the mixing is small enough, the sterile neutrino may be stable on cosmological scales and can be produced through active-sterile oscillations. In this work we assume that the mixing angle is sufficiently small to avoid these effects. For a discussion in this direction see [22, 41, 42].

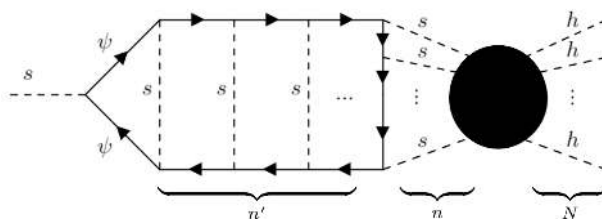


Figure 1. General radiative s decay. The values for n' refers to internal s lines in the closed fermionic loop, n for outgoing s lines and N for Higgs lines. The black globe takes into account arbitrary interactions among s and h fields.

with the mass of the scalars given by

$$m_h^2 = 2v_H^2 \lambda_H, \quad (2.4)$$

$$m_s^2 = \mu_s^2 + \lambda_{hs} v_H^2 / 2. \quad (2.5)$$

Here we consider $m_h = 125 \text{ GeV}$. The stability of the fermion is easily recognized due to the fact that it appears in pairs in the Lagrangian. In the scalar sector s appears in pairs, forbidding its decay. The linear term in s in (2.1) imply that as $m_s \geq 2m_\psi$ the pseudoscalar may decay into a pair of ψ , whereas as $m_s < 2m_\psi$ the scalar singlet becomes stable at tree level and at all orders in perturbation theory. In the following we argument the latter fact.

The possible decay of s at an arbitrary number of loops is represented in figure 1, with the decay of s followed by a singlet fermion closed loop and the black circle representing possible interactions between an arbitrary number of s and h . In the figure n' , n and N simply represent the number of the corresponding scalar lines depicted in figure 1. For simplicity, let us start assuming $n' = 0$. If n is even, the resulting fermion trace will at most contain terms of the form $\epsilon^{\mu\nu\rho\cdots} p_\mu p_\nu p_\rho \dots$, which vanishes exactly. If n is odd, the trace is different than zero, but there is no way to connect an odd number of outgoing s with an arbitrary number of N Higgs boson in the black bloop, due to the presence of the CP symmetry of the scalar potential. Now, if $n' \neq 0$, the previous arguments still remains, because internal lines of s in the fermion loop only add an even number of both γ^5 and fermion propagators to the trace, only adding vanishing contributions without changing the final result. In consequence, from a perturbative point of view, the stability is guaranteed for the pseudoscalar singlet.²

²One can introduce an axion-like anomalous 5-dimensional effective operator that conserves CP [43], $\mathcal{L} \supset \frac{\lambda}{\Lambda} s G_{\mu\nu} \tilde{G}^{\mu\nu}$, with λ a dimensionless coupling, Λ some high energy scale, G the field strength of any gauge field and \tilde{G} its dual. This operator induce the decay of the pseudoscalar singlet into gauge bosons. For instance, considering $m_s = 10^3 \text{ GeV}$, we require $\lambda \lesssim 10^{-7}$ for a Planck scale induced operator in order to have a cosmologically stable particle. For a GUT scale induced operator we require $\lambda \lesssim 10^{-10}$. Other possible low energy origin of such operator requires the introduction of heavy vector-like fermions [44], which are not part of our model construction.

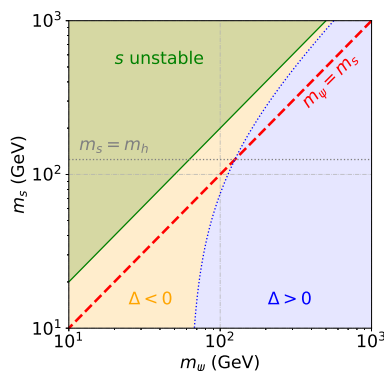


Figure 2. Mass plane, with the green region indicating s unstable, whereas in the orange and blue regions both singlets are stable. The blue one indicates where s -channel semi-annihilations are present, with $\Delta \equiv 2m_\psi - m_s - m_h \geq 0$ (for details see section 3.2).

Finally, theoretical constraints put bounds on the free parameters of the model. The stability of the electroweak vacuum for s and h imposes that [45]

$$\lambda_s > 0, \quad \lambda_{hs} > -\sqrt{\frac{2}{3}}\lambda_H\lambda_s, \quad (2.6)$$

with $\lambda_H = m_h^2/(2v_H^2) \simeq 0.1$. From perturbativity we set that $|g_\psi|, |\lambda_s| < 4\pi$ to ensure that loop corrections are smaller than tree-level processes [45]. Unitarity constraints are less stringent than the upper limits based on our perturbativity criteria [5, 46]. The signs of g_ψ and λ_{hs} are not relevant for the analysis in this work due to the fact that the relevant processes depend quadratically on them, therefore the theoretical constraints set $0 < \lambda_{hs} < 4\pi$ and $0 < g_\psi < 4\pi$.

3 Relic density

3.1 Parameter space

Depending on the intensity of the couplings and the mass hierarchy between m_ψ and m_s , the model may present different DM scenarios with one or two stable particles. When λ_{hs} takes very small values, i.e. $\lambda_{hs} \sim 10^{-12} - 10^{-6}$, the singlet sector never thermalize with the SM, then the DM production may occurs via freeze-in and/or dark freeze-out [42, 47]. On the contrary, as the Higgs portal coupling takes sizable values, the singlet scalar enters into thermal equilibrium with the SM (this work). Based on the latter fact, two possible coupling regimes concerning g_ψ may be present:

- $g_\psi \lesssim 10^{-6}$: the two singlets in the dark sector will interact feebly. If $m_s > 2m_\psi$, s becomes unstable, and ψ may be produced via freeze-in through the decay of s and $2 \rightarrow 2$ scattering processes. The green region in figure 2 shows this parameter space in terms of the mass hierarchy. For $m_s \leq 2m_\psi$, s becomes stable and define a DM candidate identical to that of the *Singlet Higgs Portal* model (SHP) [5, 8], since ψ does not interfere in the dynamic of the former due to their feebly interactions. The SHP model has been exhaustively studied previously, and displays a highly constrained parameter space around the EW scale.

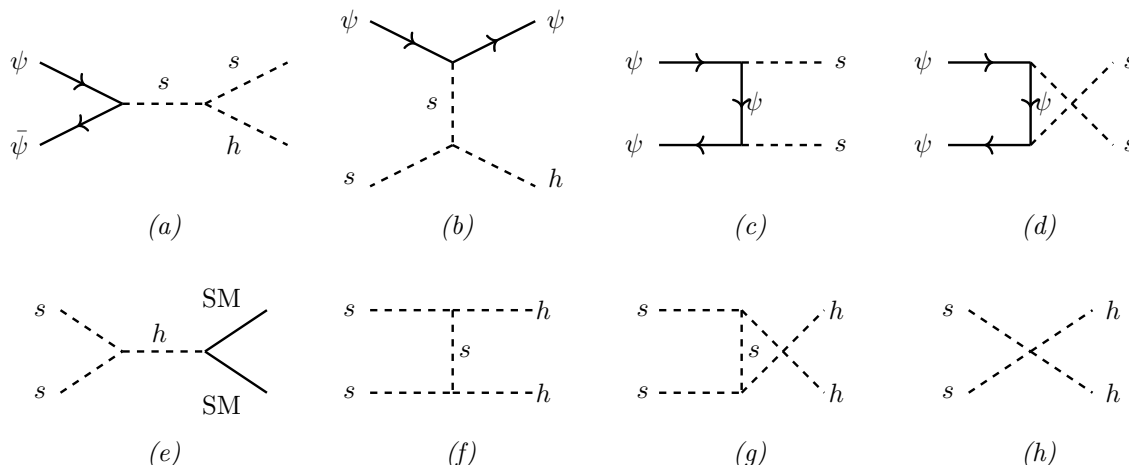


Figure 3. Relevant processes at the freeze-out time in the two DM component model. Diagrams (a) and (b) are the s - and t -channel semi-annihilations, respectively, (c) and (d) correspond to DM conversions, and (e) to (h) are the annihilations of the pseudoscalar into SM and Higgs particles.

- $g_\psi \gtrsim 10^{-6}$: s will bring ψ fast into the thermal equilibrium. From the relic abundance point of view, the only relevant case here is when both singlets are stable, i.e. $m_s < 2m_\psi$ (orange and blue region in figure 2), otherwise ψ would not have any channel to annihilate, giving rise to an overabundance (see Feynman diagrams in figure 3). Based on the latter point, different type of interactions appear that determine the relic abundance of each singlet.

In this work, we focus on this last scenario in which both singlets are stable. It is worth to mention that even when the first case with one DM candidate via freeze-in is a perfectly viable DM model, it presents a challenge phenomenology [48] (see however [49]). Recently, novel scenarios with *inverse semi-production* have been proposed with interesting dark matter production and phenomenology [50, 51].

3.2 Boltzmann equation

As we pointed out before, the two-component scenario of our interest occurs for $m_s < 2m_\psi$ and when the couplings (g_ψ, λ_{hs}) are sizable. In this case, at temperatures higher than the individual masses of the singlet, both DM components are in thermal equilibrium with the SM. The departure of the equilibrium occurs once the temperature goes below the masses of the singlets, and three types of scattering participate in this process: annihilations, semi-annihilations, and dark matter conversions (figure 3). Based on [52], the evolution of the individual singlet abundances $Y_i \equiv n_i/s$, with $i = \psi, s$, as a function of the temperature

$x \equiv \mu/T$, with $\mu = m_\psi m_s / (m_\psi + m_s)$, are given by

$$\begin{aligned} \frac{dY_\psi}{dx} &= -\lambda_{\psi\bar{\psi}ss} \left(Y_\psi^2 - Y_s^2 \frac{Y_{\psi,e}^2}{Y_{s,e}^2} \right) - \lambda_{\psi\bar{\psi}sh} \left(Y_\psi^2 - Y_s^2 \frac{Y_{\psi,e}^2}{Y_{s,e}^2} \right), \\ \frac{dY_s}{dx} &= -\lambda_{ssXX} \left(Y_s^2 - Y_{s,e}^2 \right) + \lambda_{\psi\bar{\psi}ss} \left(Y_\psi^2 - Y_s^2 \frac{Y_{\psi,e}^2}{Y_{s,e}^2} \right) \\ &\quad + \frac{1}{2} \lambda_{\psi\bar{\psi}sh} \left(Y_\psi^2 - Y_s^2 \frac{Y_{\psi,e}^2}{Y_{s,e}^2} \right) - \frac{1}{2} \lambda_{s\psi\psi h} (Y_s Y_\psi - Y_\psi Y_{s,e}), \end{aligned} \quad (3.1)$$

where we have defined

$$\lambda_{ijkl}(x) := \frac{\langle \sigma_{ijkl} v \rangle(x) \cdot s(T)}{x \cdot H(T)}, \quad \text{for } i, j, k, l = \psi, s, h, X. \quad (3.2)$$

with X referring to a SM particle, $\langle \sigma v \rangle$ the thermally averaged cross section, and the entropy density s and Hubble rate H in a radiation dominated universe given by

$$H(T) = \sqrt{\frac{4\pi^3 G}{45} g_*(T)} \cdot T^2, \quad s(T) = \frac{2\pi^2}{45} g_{*s}(T) \cdot T^3, \quad (3.3)$$

where G is the Newton gravitational constant, and g_* and g_{*s} are the effective degrees of freedom contributing respectively to the energy and the entropy density at temperature T [53]. The equilibrium densities, $Y_{i,e} \equiv n_{i,e}/s$, are calculated using the Maxwell-Boltzmann distribution, whose number density is given by

$$n_{ie}(T) = g_i \frac{m_i^2}{2\pi^2} T K_2 \left(\frac{m_i}{T} \right), \quad (3.4)$$

with g_i the internal spin degrees of freedom, and K_2 is the modified Bessel function of the second kind. The DM density parameter is given by

$$\Omega h^2 = \sum_{i=\psi,s} \Omega_i h^2, \quad \Omega_i h^2 = \frac{2.9713 \cdot 10^9}{10.5115 \text{ GeV}} \cdot Y_{i,0} \cdot m_i, \quad (3.5)$$

where $Y_{i,0}$ is the yield of each DM component today, i.e. after freeze-out.

In the following we analyze the behavior of the relic abundance obtained by solving eq. (3.1) making use of `micrOMEGAs 5.2.7a` [52], which calculates automatically all $\langle \sigma v \rangle$ in eq. (3.1). We pay special attention to those regions in which $\Omega_s h^2$ acquires smaller values than in the SHP [5] for a fixed (m_s, λ_{hs}) . This will be a necessary requirement in order to evade stringent direct detection bounds on the pseudoscalar DM from a few GeV to the TeV scale. Due to the subtle behavior of semi-annihilations in the t -channel, we divide the analysis in two parts depending on the relative hierarchy between m_s and m_h . Finally, for convenience, we introduce a new parameter $\Delta \equiv 2m_\psi - m_s - m_h$, such that as $\Delta \geq 0$ s -channel semi-annihilations are present in the relic abundance calculation. This is represented in blue in figure 2.

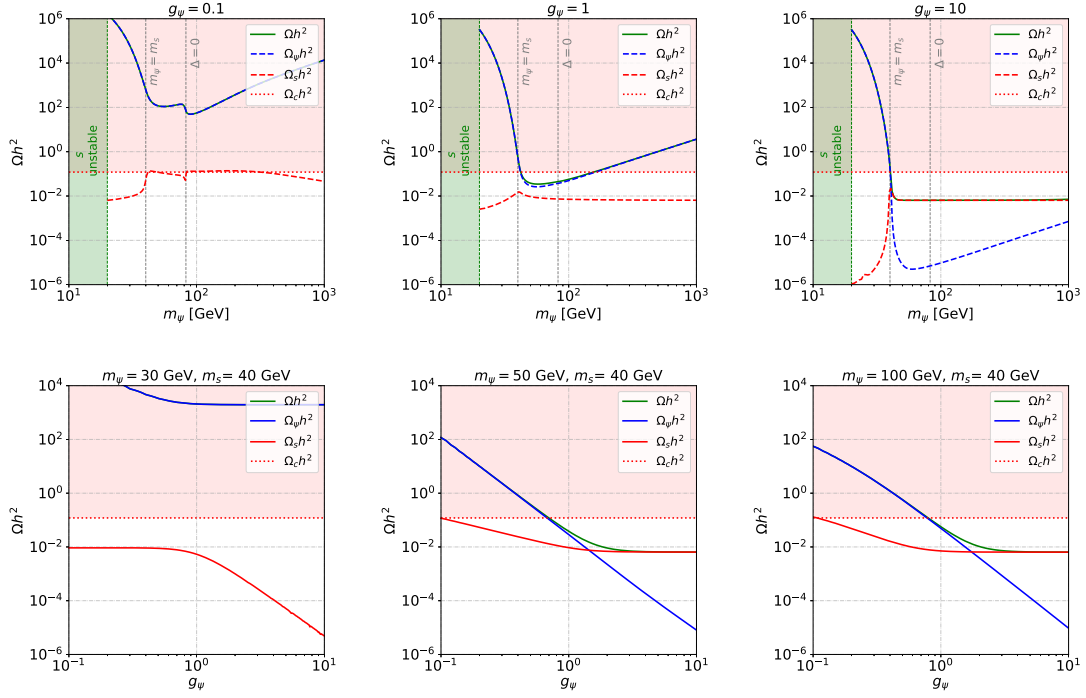


Figure 4. (*above*) Relic abundance for $m_s = 40$ and $\lambda_{hs} = 1$, for different values of g_ψ specified at the top of each plot. The green and red region are forbidden by the instability of s and relic overabundance. The vertical dashed grey lines remark the points at which $m_\psi = m_s$ and $\Delta = 0$. (*below*) Relic abundance as a function of g_ψ for $m_s = 40$ and $m_\psi = 30, 40$ and 100 GeV, respectively, with $\lambda_{hs} = 1$.

3.2.1 $m_s < m_h$

In this region all the processes in figure 3 may be present but the semi-annihilation in the t -channel. Now, when m_ψ is small enough, i.e. $\Delta < 0$, then the s -channel semi-annihilation is not present either, and only pseudoscalar annihilations and DM conversions are present. Normally in this regime, an overabundance occurs as $m_s > m_\psi$, since ψ does not have effective annihilation channels. As $m_\psi > m_s$, DM conversions of the type $\psi\bar{\psi} \rightarrow ss$ become effective, decreasing the overabundance of Ω_ψ . If m_ψ is big enough such that $\Delta \geq 0$, semi-annihilations in the s -channel become efficient, decreasing Ω_ψ even more. These characteristics can be seen in figure 4 (*above*), where the abundances are depicted as a function of m_ψ , for $m_s = 40$ GeV, $g_\psi = (0.1, 1, 10)$ and $\lambda_{hs} = 1$, with the green and red regions representing s unstable and DM overabundance, respectively. The effects of conversions at $m_\psi = m_s$ becomes sharper as g_ψ increases, since $\langle \sigma_{\psi\psi ss} v \rangle \sim g_\psi^4$ (see appendix A). Equivalently, s -channel semi-annihilations near $\Delta = 0$ pushes down Ω_ψ , and since both conversions and s -channel semi-annihilations depends inversely on m_ψ^2 , their effectiveness decreases with the growing of m_ψ , then making Ω_ψ to increase for higher values of m_ψ . The changes of Ω_s are stronger only for $m_s > m_\psi$, where $ss \rightarrow \psi\bar{\psi}$ conversions are effective, and due to $\langle \sigma_{ss\psi\psi} v \rangle \propto g_\psi^4$, Ω_s decreases notoriously for such high couplings g_ψ shown in the figure 4 (*above*) right plot. We do not show the dependence of the relic

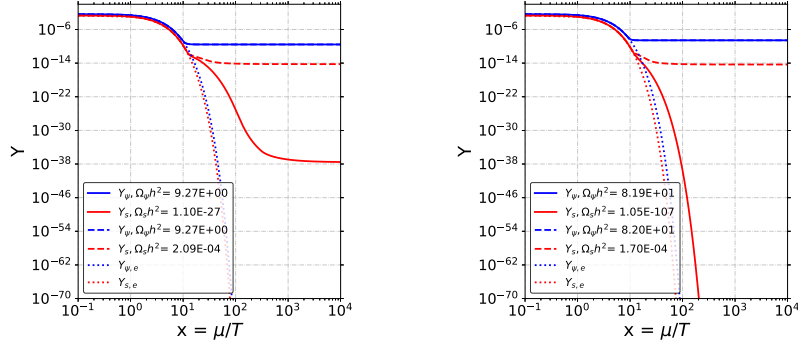


Figure 5. DM yields as a function of x in the region $m_s > m_h$ and $\Delta < 0$, considering (continuous lines) and not (dashed lines) the t -channel semi-annihilation. In both cases we have set $m_s = 130$ GeV and $g = \lambda_{hs} = 1$, with $m_\psi = 120$ GeV (*left*) and $m_\psi = 110$ GeV (*right*). In the legends are specified the parameter densities for each case. The dotted lines correspond to the equilibrium densities of each singlet.

abundances on λ_{hs} , but the changes are minor due to the fact that this parameter affects only the semi-annihilation intensity and modulates Ω_s .

In figure 4 (*below*) we show the abundances as a function of g_ψ , keeping $\lambda_{hs} = 1$. The relic abundance behavior depends strongly on the mass hierarchy and the magnitude of g_ψ . As it was previously discussed, for $m_\psi < m_s$ (left plot) it is Ω_ψ that dominates the relic, independently of g_ψ . In this case, λ_{hs} would only change the relative abundance of the scalar singlet, but keeping very high values for Ω_ψ . Oppositely, in the cases $m_\psi > m_s$ (middle and right plot), the relic hierarchy do depends on g_ψ , showing the effectiveness of conversions and s -channel semi-annihilation, respectively, with a notorious fall of Ω_ψ in each case.

3.2.2 $m_s > m_h$

In this case, the t -channel semi-annihilation $\psi + s \rightarrow \psi + h$ is present, and it may participates strongly in the determination of Y_s for $\Delta < 0$. The effectiveness of this semi-annihilation on Y_s becomes highly sharp, due to the fact that once both DM components decouple from the SM plasma, Y_s follows in a good approximation

$$\frac{dY_s}{dx} \propto -\frac{1}{2}x^{-2}\lambda_{s\psi\psi h}Y_\psi Y_s, \quad x \gtrsim 10, \quad (3.6)$$

assuming $Y_\psi \approx \text{constant}$ and $Y_{s,e} \approx 0$. The solution of eq. (3.6) gives an exponential suppression for Y_s , highly sensitive to the mass difference between the singlets. As an example of this behavior, in figure 5 we show the evolution of the densities Y_ψ (blue lines) and Y_s (red curves) as a function of $x = \mu/T$, for $m_s = 130$ GeV, and $m_\psi = 120$ GeV (left plot) and 110 GeV (right plot). As figure 5 (*left*) suggests, Y_s depends strongly on the t -channel semi-annihilation, and this can be noted by the dashed and solid red curves, with the former not considering the process in the Boltzmann equation and the latter containing it. As the mass difference between the two singlets increases, the effects becomes sharper,

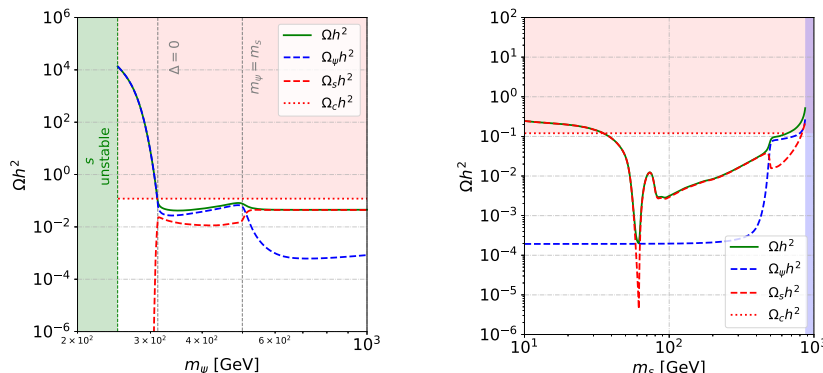


Figure 6. (left) Relic abundance as a function of m_ψ , for $m_s = 500$ GeV, $g_\psi = 10$ and $\lambda_{hs} = 0.25$. (right) Relic abundance as a function of m_s , for $m_\psi = 500$ GeV, and the same couplings than in the left plot. The blue region in the right corresponds to $\Delta < 0$.

as shown in figure 5(right). Y_ψ is almost independent on this process, as it can be seen through the overlapping of the dashed and solid blue lines. This effect is particularly interesting due to the fact that as Ω_s becomes negligible, no direct detection bounds will apply on the pseudoscalar DM. This behavior was also seen in a two-component DM model consisting of two complex scalars stabilized by a Z_5 symmetry [54].

For $\Delta > 0$, the two semi-annihilations enter into the coupled Boltzmann equations, and it is not longer possible to assume Y_ψ constant, therefore eq. (3.6) is not a good approximation to determine Y_ψ . In figure 6 we show the dependence of the relic abundance as a function of m_ψ (left) and m_s (right). Contrary to the case in the low mass regime of figure 4, in the left plot of figure 6 we observe that conversions occur at higher values of m_ψ than s -channel semi-annihilations. When the latter channel becomes efficient, the total relic abundance decreases in various order of magnitude. There is an interesting effect we want to point out, namely the fall of Ω_s as $m_s \gtrsim m_\psi$. In both plots of figure 6 is possible to observe this effect, but in the right plot is more clear the role that conversions are playing, with the red dashed line making a tiny well from the soft growing as m_s increases (i.e. $m_s \gtrsim 500$ GeV). This is, conversions of the type $ss \rightarrow \psi\psi$ start to be effective making a deviation from the well known behavior of the SHP [5] (for works with related behaviors see [36, 55, 56]). This type of wells, along with the Higgs resonance at $m_s \approx m_h/2$, will be of particular importance to evade direct detection constraints.

In conclusion, we have analyzed the effectiveness of annihilations, conversions and semi-annihilations on the relic abundance of ψ and s in the parameter space. A random scan under theoretical and experimental constraints becomes useful in order to explore in major detail the viable regions of the model, and this is what we analyze in section 4.

4 Phenomenology

In this section we present the relevant experimental constraints on the model along with a full scan of the parameter space. Once obtained the allowed parameter space, we explore indirect signals and we set upper limits from it.

4.1 Experimental constraints

When $m_s \leq m_h/2$, the Higgs boson can decay into two s DM particles, with a decay width given by

$$\Gamma_{\text{inv}}(h \rightarrow ss) = \frac{\lambda_{hs}^2 v_H^2}{32\pi m_h} \sqrt{1 - \frac{4m_s^2}{m_h^2}}. \quad (4.1)$$

This contributes to the invisible branching rate $\text{Br}(h \rightarrow \text{inv}) = \Gamma_{\text{inv}}/(\Gamma_{\text{SM}} + \Gamma_{\text{inv}})$, where the total decay width of the Higgs into SM particles is given by $\Gamma_{\text{SM}} = 4.07 \text{ MeV}$ [57]. Experimental searches put stringent constraints on this quantity, and the most strict value is given by $\text{Br}(h \rightarrow \text{inv}) < 0.19$ at 95% C.L. [57].

From the DM sector we have the following constraints. First, the measurement of the DM relic density today, given by $\Omega_c h^2 = 0.120 \pm 0.001$ [58]. Based on the uncertainties in our computation, we apply this constraint with a tolerance of $\sim 10\%$, i.e. $\Omega_c h^2 \in [0.11, 0.12]$. Secondly, direct detection, which in multicomponent DM scenarios the interaction of DM with nucleus matter through the spin-independent (SI) cross section comes from weighting it by a factor which takes into account the relative abundance Ω_i over the Planck measured Ω_c , i.e.,

$$\hat{\sigma}_{\text{SI},i} = \left(\frac{\Omega_i}{\Omega_c} \right) \sigma_{\text{SI},i}, \quad i = \psi, s, \quad (4.2)$$

where $\sigma_{\text{SI},i}$ is the spin-independent cross section. At tree level, it is only the pseudoscalar DM which interacts with nuclei via the Higgs portal, with its SI cross section given by [5]

$$\sigma_{\text{SI},s} = \frac{\lambda_{hs}^2 f_N^2}{4\pi} \frac{\mu_i^2 m_n^2}{m_h^4 m_s^2}, \quad (4.3)$$

with m_n as the nucleon mass, f_N is a factor proportional to the nucleon matrix elements, and $\mu = m_n m_s / (m_n + m_s)$ is the DM-nucleon reduced mass. Upper bounds on σ_{SI} are given by XENON1T data [59] and the projections of XENONnT [60].

4.2 Scan

In this section we show a scan on the parameter space in the range $m_{\psi,s} \in [10, 1000] \text{ GeV}$ (subject to $m_s < 2m_\psi$) and $g_\psi, \lambda_{hs} \in [0.001, 4\pi]$. The full scan highlight interesting features that were already anticipated in section 3.2. In figure 7 we show the scan of points projected on the plane (m_ψ, m_s) , with the density color representing the total abundance Ωh^2 (left), $\Omega_\psi h^2$ (middle) and $\Omega_s h^2$, respectively. The green region (top left) corresponds to those points with $m_s > 2m_\psi$, then making s unstable. We pay attention to four regions based on figure 7 (left):

- (a) *Dark red band.* In general, Ω_ψ get too big values for $m_\psi < m_s$, since no effective annihilation channels for the singlet fermion are present (see section 3.2.1). However, there is a smooth relic density transition from the deep red to lower relic densities, due to the thermal tail distribution of conversions and s -channel semi-annihilation as $\Delta \lesssim 0$. With respect to Ω_s , it is always sub-abundant, specially for $m_s > m_h$ where the t -channel semi-annihilations are present, and as we have described in section 3.2.2, tiny mass shift between ψ and s makes Ω_s to decrease strongly (deep blue region in figure 7 (right)).

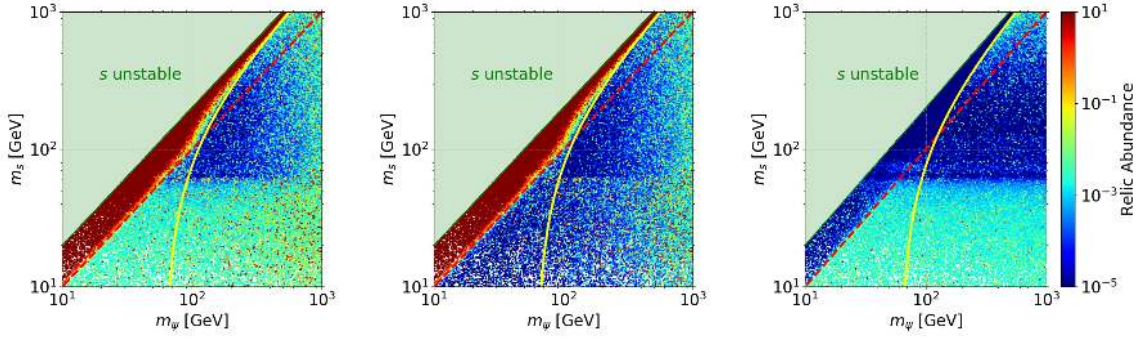


Figure 7. Random scan points projected in the mass plane with the bar color indicating the total relic abundance Ωh^2 (left), $\Omega_\psi h^2$ (middle) and $\Omega_s h^2$ (right). The homogeneous green region in the top left of each plot corresponds to s unstable, i.e. $m_s > 2m_\psi$. The red dashed line indicates $m_\psi = m_s$ and the yellow one the frontier $\Delta = 0$.

- (b) *Green area in below.* In this region the relic is mostly dominated by the pseudoscalar, as it can be seen from the plots. As it was shown in figure 4, $\Omega_\psi < \Omega_s$ for conversion-driven processes of the type $\psi\bar{\psi} \rightarrow ss$ and moderate couplings ($g_\psi \sim 1$). For very high m_ψ is possible to observe that Ω_ψ tend to increase, as conversions and semi-annihilations are less effective.
- (c) *Higgs resonance and thresholds.* In the region $50 \text{ GeV} \lesssim m_s \leq m_h$ the Higgs resonance and SM thresholds are present, then pseudoscalar annihilations are enhanced. These effects are more clear in figure 7 (right) for Ω_s . For $m_s \lesssim m_h/2$, s -channel annihilations of the singlet pseudoscalar via Higgs resonance tend to be very effective, decreasing Ω_s substantially, as it can be seen with the deep blue horizontal line. For $m_h/2 < m_s < m_W$ the abundance of s lift up, and for $m_s \lesssim m_W$ the relic decreases again. The thresholds at m_Z and m_h are also present but they are less notorious.
- (d) *Blue-green upper region.* For the singlet masses $\gtrsim 100 \text{ GeV}$, the relic of both components tends to be low (blue points), but as the masses increase the effectiveness of conversions and semi-annihilations become less strong, i.e. $\langle\sigma v\rangle \sim m_{\psi,s}^{-2}$ (appendix A), then raising the relic of both components. In this mass region the relic abundance seems to acquire moderate values in order to fulfill the Planck measurement.

The conjunction of the three plots suggests that most of the points that could give the correct relic abundance are just in very specific sectors, and those regions must to shrink even more when other constraints are taken into account. In figure 8 (left) we show the resulting parameter space points after imposing the constraints from relic abundance, Higgs to invisible and direct detection bounds. Specifically, the regions are: (i) Higgs resonance, (ii) region with $m_s > m_h$ and $\Delta < 0$, and (iii) in the high mass with $\Delta > 0$ and $m_\psi < m_s$, indicating the corresponding Ω_ψ with a color bar. Region (i) is the only one that allows $m_\psi > m_s$ and where the Higgs to invisible constraint applies.³ The points in region (ii) eas-

³In the presence of a resonance, the smallness of the Higgs portal coupling may breakdown the assumption of local thermal equilibrium when chemical decoupling is taking place. In our case we have not considered those effects, where a more involved treatment must be carried [61].

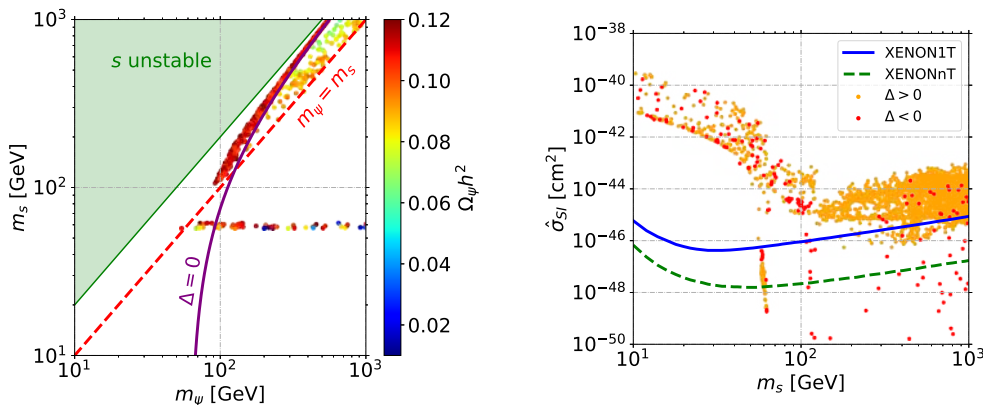


Figure 8. (left) Points fulfilling direct detection and relic abundance in all the scanned parameter space. (right) The same selected random points shown in the left plot, now projected on $(m_s, \hat{\sigma}_{SI,s})$, where we distinguish points with $\Delta > 0$ (orange) and $\Delta < 0$ (red). The continuous blue line corresponds to the upper limit given by XENON1T (1 t.y) [59], whereas the green dashed line a projection for XENONnT (20 t.y) [60].

ily evade XENON1T constraints due to the fact that $\Omega_s \rightarrow 0$, then the condition $\Omega_\psi = \Omega_c$ is enough to fulfill all the experimental constraints. Finally, in the high mass region we found some points anticipated by the analysis around figure 6, where the power of conversions and s -channel semi-annihilations makes Ω_s to decrease enough evading XENON1T. The cost of the latter implies values for g_ψ near the perturbativity limit criteria (this point is discussed in the last section). In figure 8 (right) we project the scan points on the plane $(m_s, \hat{\sigma}_{SI,s})$, contrasted with the limits given by XENON1T and the XENONnT projection [60]. Even when XENON experiments rule out most of the orange points (i.e. regions (i) and (iii)), a fraction of red points ($\Delta < 0$ and $m_s > m_h$) easily evade the strongest direct detection constraints. It is worth to say that this inverted peak at the Higgs resonance is a typical characteristic of Higgs portals, hardly to be ruled out by experiments.

To end this subsection, we would like to point out about the limitations of our random scan, which was based on overlaying exclusion limits (mainly from relic abundance and direct detection). It is well known that this type of exclusions present some drawbacks, such as the blindness to the influence of the choice of some parameters (e.g. DM halo distribution or the Higgs mass pole) on the experimental limits, or the fact that the *allowed regions* do not present additional information about which points are more favored than others. Considering those limitations, statistical analysis based on combined likelihoods functions may give a more accurate and realistic way to cure those disadvantages, although beyond the scope of the present analysis [8, 62].

4.3 Indirect detection

In the previous subsection we found that three regions of the parameter space fulfill invisible Higgs decay, relic abundance and direct detection constraints, with two of them being practically in the region $\Delta > 0$. In that case, s -channel semi-annihilations are expected

to give sizable fluxes of particles today through its s -wave nature. The t -channel semi-annihilation also goes in the s -wave, but we have checked that in general its cross section is lower than the corresponding s -channel, and indirect signals with a pair of s in the initial state have shown to be not sizable outside the Higgs resonance [5]. Additionally, $\Omega_\psi h^2$ reaches $\sim 50\%$ to 99% of the total DM budget in the high mass regime (see figure 8(left)), consequently the scaling factor $(\Omega_\psi/\Omega_c)^2$ does not considerably suppress the flux produced by the s -channel semi-annihilation. In the following, we show the box-shaped differential spectra [63] for this channel with its subsequent decay $h \rightarrow \gamma\gamma$, and secondly, restrictions on the parameter space coming from bounds based on searches of gamma rays (Fermi-LAT), anti-protons (AMS-02), and projections from the Cherenkov Telescope Array (CTA) are presented.

4.3.1 Box-shape gamma ray

The differential flux of photons produced in fermionic DM annihilations and received at earth from a given solid angle in the sky $\Delta\Omega$ with a detector of area A is given by

$$\frac{d\Phi_\gamma}{dE_\gamma} = \frac{1}{A} \frac{dN_\gamma}{dE_\gamma dt} = \frac{\langle\sigma_{sh}v\rangle}{8\pi m_\psi^2} \left(\text{Br}_h \frac{dN}{dE_\gamma} \right) \left(\frac{1}{\Delta\Omega} \int_{\Delta\Omega} J d\Omega \right), \quad (4.4)$$

where $\langle\sigma_{sh}v\rangle$ is the corresponding average annihilation cross section times velocity of the process $\psi + \bar{\psi} \rightarrow s + h$, Br_h is the branching ratio of the Higgs into two photons, and dN/dE_γ the corresponding normalized spectra. The J factor is the integral of the squared DM density ρ_{DM} along the line of sight $J = \int_{\text{l.o.s.}} ds \rho_{\text{DM}}^2$. We consider as our main region of interest the galactic center, which features $\Delta\Omega = 1.30$ sr, $\int_{\Delta\Omega} J d\Omega = 9.2 \times 10^{22} \text{ GeV}^2 \text{cm}^{-5}$, assuming a NFW profile normalized to a local DM density of 0.4 GeV/cm^3 [64]. To determine the normalized spectra of emitted photons, we first note that their energies, in the fermion DM collision frame,⁴ are given by

$$E_{\gamma,1} = \frac{m_h^2/2}{E_h - \sqrt{E_h^2 - m_h^2} \cos \theta}, \quad E_{\gamma,2} = E_h - E_{\gamma,1}, \quad (4.5)$$

where θ corresponds to the angle sustained by one of the photons and the in-flight Higgs. The energy of the emitted scalar particles in the rest frame of the collision of ψ are given by

$$E_h = m_\psi \left(1 - \frac{m_s^2 - m_h^2}{4m_\psi^2} \right), \quad E_s = m_\psi \left(1 + \frac{m_s^2 - m_h^2}{4m_\psi^2} \right). \quad (4.6)$$

For a fixed E_h , the energy of the photon received at earth depends only on θ , with a maximum (minimum) energy for $\theta = 0(\pi/2)$,⁵ then displaying a box-shaped spectrum centered at $E_c \equiv (E(0) + E(\pi))/2 = E_h/2$ and with a width $\Delta E \equiv E(0) - E(\pi) =$

⁴Today, fermion DM ψ moves non-relativistically, therefore colliding practically in the earth rest frame.

⁵It is possible to receive the two photons at earth as $\theta \rightarrow 0$, or equivalently, when both photons are emitted transverse to the Higgs direction. This scenario requires a highly boosted Higgs and a detailed analysis of the emitted photons.

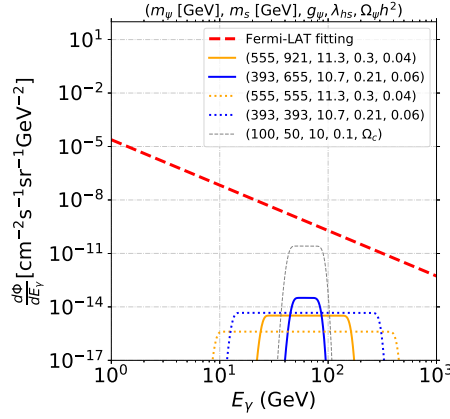


Figure 9. Differential gamma ray flux originated in the galaxy center from the process $\psi + \bar{\psi} \rightarrow s + h$, followed by the decay $h \rightarrow \gamma\gamma$, for two random points fulfilling relic abundance and direct detection (continuous lines), whereas the dotted curves represent hypothetical points in which the two DM components are completely degenerated. The dashed red line corresponds to the flux given by Fermi-LAT [63], and the gray an hypothetical point with low (m_ψ, m_s) .

$\sqrt{E_h^2 - m_h^2}$. Therefore, the normalized spectra can be written as⁶

$$\frac{dN}{dE_\gamma} = \frac{2}{\Delta E} \Theta \left(E_\gamma - E_c + \frac{1}{2} \Delta E \right) \Theta \left(E_c + \frac{1}{2} \Delta E - E_\gamma \right), \quad (4.7)$$

where the factor multiplicative factor 2 accounts for the two emitted photons (then E_γ any of the two photons in (4.5)), and Θ are Heaviside functions.

In figure 9 (left) we show the box-shaped spectra for two random points allowed by the relic density abundance and XENON1T, contrasted with the data given by Fermi-LAT (red dashed line), where we have taken the background fitting function in order to estimate the data signal: $d\Phi_\gamma/dE = 2.4 \times 10^{-5} (E_\gamma/\text{GeV})^{-2.55} \text{GeV}^{-1} \text{cm}^{-2} \text{s}^{-1} \text{sr}^{-1}$ [64]. As it was anticipated above, the differential fluxes for the selected points are well below the red dashed line, in principle not showing any possible tension. The blue and orange dot curves show the spectra when the two DM components become degenerated, widening the boxes and therefore peaking at higher energy. Only points with masses (and high couplings) as small as $m_\psi \sim 100 \text{ GeV}$ may approach significantly to the red dashed line, as it is depicted by the grey dashed line in figure 9 (left). It is known that the power of box-shaped gamma rays goes in their potential deviation with respect to the power-law Fermi-LAT background, then the previous result is premature to discard a possible constraint on the parameter space. In order to do this, in the following we use the recent upper bounds on gamma rays produced in semi-annihilations based on Fermi-LAT data, along with anti-protons flux measurements.

⁶Note that in the ψ annihilation center-of-mass frame, due to the conservation of angular momentum, the two photons must be emitted back to back if they have the same polarization, and co-linearly if they have opposite polarization; the conservation of linear momentum requires s to be emitted along with one of the photons in the former case, and in the direction opposite to the photons in the latter. See also [65].

4.3.2 Upper bounds

Upper limits on $\langle\sigma_{hs}v\rangle$ have not been constructed yet in order to constraint the parameter space via indirect searches. However, they can be inferred from existing upper bounds on the average annihilation cross section times velocity for $DM + DM \rightarrow DM + h$ process based on gamma-ray signals [66], and from $DM + DM \rightarrow b\bar{b}(W^+W^-)$ based on anti-proton flux measurements [67]. In the following we derive the useful algebraic relations to translate the existing upper bounds to our average semi-annihilation cross section times velocity $\langle\sigma_{sh}v\rangle$.

First, let us consider the process $\psi\bar{\psi} \rightarrow \psi'h$, with ψ and ψ' arbitrary DM particles, and h the Higgs boson. This process presents an average cross section times relative velocity given by

$$\langle\sigma_{\psi'h}v\rangle = \frac{16\pi}{J} m_\psi^2 \Phi_h, \quad \text{with} \quad E_h = m_\psi \left(1 - \frac{m_{\psi'}^2 - m_h^2}{4m_\psi^2}\right) \quad (4.8)$$

with J an arbitrary J -factor, m_ψ the mass of the initial states, Φ_h is the flux, and the outgoing Higgs having an energy E_h (equivalently to (4.6)). Now, it is possible to have the same flux Φ_h with an outgoing Higgs having the same energy E_h in another process given by $\psi\bar{\psi} \rightarrow hh$:

$$\Phi_h = \frac{1}{2} \frac{\langle\sigma_{hh}v\rangle}{8\pi E_h^2} J, \quad (4.9)$$

where the $1/2$ factor comes from the fact that we are considering one outgoing Higgs, and we have set $m_\psi = E_h$. Combining (4.8) and (4.9) we obtain

$$\langle\sigma_{\psi'h}v\rangle = \frac{1}{(1 - \xi_{\psi'})^2} \langle\sigma_{hh}v\rangle, \quad (4.10)$$

with $\xi_x \equiv (m_x^2 - m_h^2)/(4m_\psi^2)$, with x being some particle in the final state. From the last relation ψ' is an arbitrary state, then in eq. (4.10) taking $\psi' = \psi$ and $\psi' = s$ and combining the resulting expressions, it follows that

$$\left(\frac{1 - \xi_s}{1 - \xi_\psi}\right)^2 \langle\sigma_{sh}v\rangle = \langle\sigma_{\psi h}v\rangle, \quad (4.11)$$

Upper limits on $\langle\sigma_{\psi h}v\rangle$ [66], now can be compared to our $\langle\sigma_{sh}v\rangle$ for certain values of m_ψ and m_s through eq. (4.11). In figure 10 (*top row*) we show the projection of under-abundant points (green) and those that give approximately the correct relic abundance (blue points) for the resulting average annihilation cross section times velocity (left side of eq. (4.11)) times the relative abundance of the annihilating DM particles. The red line in both plots corresponds to the upper bound found in [66] (right side of eq. (4.11)). All these points are in the region $\Delta > 0$ and fulfill direct detection constraints. None of the bounds touch the parameter space points, then not showing any possible exclusion. Note that the blue points well below the upper bounds (red line) correspond to the Higgs resonance region, since lower couplings (g_ψ, λ_{hs}) are necessary to compensate the resonance effect, then reducing the ID signals.

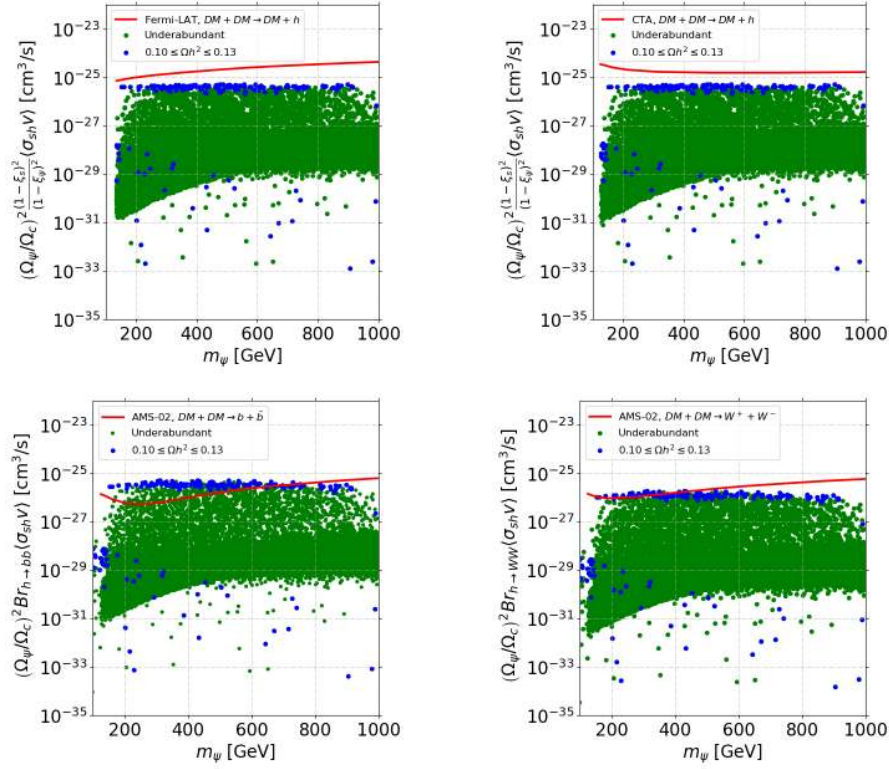


Figure 10. Points with $\Delta > 0$ fulfilling direct detection constraints as a function of the re-scaled average annihilation cross section times velocity given by expressions (4.11) and (4.14) multiplied by the relative abundance $(\Omega_\psi/\Omega_c)^2$ of the annihilating fermion DM. Upper bounds for Fermi-LAT [66], CTA [66] and AMS-02 [67] are given by the red continuous lines. For details see the main text.

On the other hand, AMS-02 anti-protons measurement set upper bounds on $\langle \sigma_{\text{DM DM} \rightarrow X \bar{X}} v \rangle \equiv \langle \sigma_{X \bar{X}} v \rangle$ with $X \bar{X} = b \bar{b}, W^+ W^-$ [67]. From the semi-annihilation with the Higgs decaying into $b \bar{b}$ we have that

$$\text{Br}(h \rightarrow b \bar{b}) \langle \sigma_{sh} v \rangle = \frac{8\pi}{J} m_\psi^2 \Phi_{b\bar{b}} \quad (4.12)$$

Additionally, the flux $\Phi_{b\bar{b}}$ in (4.12) can be produced by an arbitrary interaction $\psi \bar{\psi} \rightarrow b \bar{b}$:

$$\Phi_{b\bar{b}} = \frac{\langle \sigma_{b\bar{b}} v \rangle}{8\pi m_\psi^2} J \quad (4.13)$$

Combining (4.12) and (4.13) we obtain

$$\text{Br}(h \rightarrow b \bar{b}) \langle \sigma_{sh} v \rangle = \langle \sigma_{b\bar{b}} v \rangle \quad (4.14)$$

Equivalently for $W^+ W^-$. In figure 9 (bottom row) we show the projection of points considering the semi-annihilation with Higgs decay into $b \bar{b}$ and $W^+ W^-$, contrasted with the upper bounds given by AMS-02. From the resulting plots, $b \bar{b}$ search set the stringent bounds on the parameter space of the model, discarding points with the correct relic abundance with masses below $\sim 500 - 700$ GeV, approximately.

5 Discussion and conclusions

In this paper we have explored a simple extension to the SM containing two gauge-singlet fields: a Dirac fermion and a real pseudoscalar. From the DM point of view, the model present multiple scenarios with one or two DM components. Previous works have focused on the scenario when the Higgs portal coupling takes very small values, in such a way that the dark sector evolves decoupled from the SM, with the DM relic abundance produced via dark freeze-out/freeze-in. In the present work we found that as the Higgs portal take sizable values it is possible to produce one-component DM candidate via freeze-in or two-component DM via freeze-out. We have focused on the latter scenario, which only presents four free parameters: two masses and two couplings.

The stability of the two singlets is guaranteed by parity arguments without the necessity of invoking additional symmetries. Furthermore, the relic abundance of both singlets is determined via freeze-out through annihilations, DM conversions and semi-annihilations. The appearance of the latter is contrary to the standard belief that this type of processes appear only in the presence of symmetries larger than Z_2 . We have explored the relic density abundance of both DM components in the parameter space, founding interesting behaviors depending on the mass hierarchy and couplings values. Semi-annihilations and DM conversions play an important role in two of the three available regions, making the pseudoscalar relic abundance low enough to evade direct detection XENON1T bounds, and then allowing DM with masses of hundreds of GeV up to the TeV scale. As it is usual with Higgs portals, the resonance region will not be discarded completely, even with the powerful projection of XENONnT.

We have complemented our analysis with indirect detection signatures and bounds. Firstly, we have explored box-shape gamma rays signals appearing from a fermion DM semi-annihilation, showing small boxes signals for the fermion DM s -channel semi-annihilation. Furthermore, we have translated bounds from gamma-ray searches from Fermi-LAT and CTA projections onto the semi-annihilation, not showing any possible tension, although the sensitivity of both experiments rely in the ballpark of part of the parameter space of the model. In fact, considering that our numerical methods are not very precise, a more detailed and sophisticated analysis such as a global-fit could be perfectly sensitive to these gamma-rays upper bounds in view of the expected quantitative differences between the two methods. As a final analysis, we have tested the model with anti-protons upper bounds from AMS-02 experiment, showing an exclusion of fermion DM masses below $\sim 500\text{--}700$ GeV (again, only when the s -channel semi-annihilation is present).

Finally, considering that the viability of the model requires high values for the dark sector coupling g_ψ in some regions of the parameter space, there are two important points to be taken into account, although the precise calculation of them are beyond the scope of the present work. The first is related to the possible appearance of Landau poles at low energy scales, implying an urgent UV completion of the model (e.g. embedding the pseudoscalar into a complex singlet which acquires vev). The second point is related to the spin-independent one-loop amplitude in direct detection for the singlet fermion, which due to the high coupling values it may give a sizable contribution, possibly excluding even more

parameter space of the model, in particular the special region in which the relic abundance of the pseudoscalar drops to zero.

Acknowledgments

We would like to thank Alejandro Ibarra, Camilo García, Alexander Belyaev and Claudio Dib for useful discussions, and to Alexander Pukhov for helping with MicrOMEGAS. B.D.S would like also to ANID (ex CONICYT) Grant No. 74200120. A.Z. has been partially funded by ANID (Chile) PIA/APOYO AFB 180002 and by ANID-Millennium Science Initiative Program - ICN2019 044. P.E. has been funded by project FONDECYT N° 1170171, Beca doctorado nacional Chile ANID and DGIIP-UTFSM. S.N. has been funded by Beca doctorado nacional Chile ANID.

A Annihilation cross sections

The exact values of $\langle\sigma v\rangle$ for the different $2 \rightarrow 2$ processes were calculated with **micrOMEGAs 5.2.7a**. In order to show the dependence of the thermally average cross section on the parameters of the model, in this appendix we show some expressions for $\langle\sigma v\rangle$ in the limit in which $\langle\sigma v\rangle \approx (\sigma v)|_{s=(m_1+m_2)(1+v^2/4)}$, with m_1 and m_2 the masses of the annihilating particles, keeping the s -wave only when it is present:

$$\langle\sigma v\rangle_{\psi+\bar{\psi}\rightarrow s+h} = \frac{g_\psi^2 \lambda_{hs}^2 v_H^2 \sqrt{-2m_h^2(m_s^2+4m_\psi^2)+m_h^4+(m_s^2-4m_\psi^2)^2}}{64\pi m_\psi^2 (4m_\psi^2-m_s^2)^2}, \quad (\text{A.1})$$

$$\langle\sigma v\rangle_{\psi+\bar{\psi}\rightarrow s+s} = \frac{g_\psi^4 m_\psi (m_\psi^2-m_s^2)^{5/2}}{24\pi (m_s^2-2m_\psi^2)^4} v^2 \quad (\text{A.2})$$

$$\langle\sigma v\rangle_{s+s\rightarrow\psi+\bar{\psi}} = \frac{g_\psi^4 (m_s^2-m_\psi^2)^{3/2} (2m_s^2+3m_\psi^2)}{60\pi m_s^7} v^4 \quad (\text{A.3})$$

$$\langle\sigma v\rangle_{\psi+s\rightarrow\psi+h} = - \frac{g_\psi^2 \lambda_{hs}^2 v_H^2 \sqrt{(m_s^2-m_h^2)((m_s+2m_\psi)^2-m_h^2)} \left(2m_\psi - \frac{-m_h^2+m_s^2+2m_s m_\psi+2m_\psi^2}{m_s+m_\psi}\right)}{32\pi m_s (m_s+m_\psi)^2 \left(m_\psi \frac{-m_h^2+m_s^2+2m_s m_\psi+2m_\psi^2}{m_s+m_\psi} + m_s^2 - 2m_\psi^2\right)^2} \quad (\text{A.4})$$

The corresponding expressions for the annihilations of a pair of s into SM particles can be found in the appendix of [5].

Open Access. This article is distributed under the terms of the Creative Commons Attribution License ([CC-BY 4.0](https://creativecommons.org/licenses/by/4.0/)), which permits any use, distribution and reproduction in any medium, provided the original author(s) and source are credited.

References

- [1] G. Bertone and D. Hooper, *History of dark matter*, *Rev. Mod. Phys.* **90** (2018) 045002.
- [2] V. Silveira and A. Zee, *Scalar phantoms*, *Phys. Lett. B* **161** (1985) 136 [[INSPIRE](#)].
- [3] J. McDonald, *Gauge singlet scalars as cold dark matter*, *Phys. Rev. D* **50** (1994) 3637 [[hep-ph/0702143](#)] [[INSPIRE](#)].
- [4] C.P. Burgess, M. Pospelov and T. ter Veldhuis, *The Minimal model of nonbaryonic dark matter: A Singlet scalar*, *Nucl. Phys. B* **619** (2001) 709 [[hep-ph/0011335](#)] [[INSPIRE](#)].
- [5] J.M. Cline, K. Kainulainen, P. Scott and C. Weniger, *Update on scalar singlet dark matter*, *Phys. Rev. D* **88** (2013) 055025 [Erratum *ibid.* **92** (2015) 039906] [[arXiv:1306.4710](#)] [[INSPIRE](#)].
- [6] Y.G. Kim, K.Y. Lee and S. Shin, *Singlet fermionic dark matter*, *JHEP* **05** (2008) 100 [[arXiv:0803.2932](#)] [[INSPIRE](#)].
- [7] M. Escudero, A. Berlin, D. Hooper and M.-X. Lin, *Toward (Finally!) Ruling Out Z and Higgs Mediated Dark Matter Models*, *JCAP* **12** (2016) 029 [[arXiv:1609.09079](#)] [[INSPIRE](#)].
- [8] GAMBIT collaboration, *Status of the scalar singlet dark matter model*, *Eur. Phys. J. C* **77** (2017) 568 [[arXiv:1705.07931](#)] [[INSPIRE](#)].
- [9] M. Pospelov, A. Ritz and M.B. Voloshin, *Secluded WIMP Dark Matter*, *Phys. Lett. B* **662** (2008) 53 [[arXiv:0711.4866](#)] [[INSPIRE](#)].
- [10] Q.-H. Cao, E. Ma, J. Wudka and C.P. Yuan, *Multipartite dark matter*, [arXiv:0711.3881](#) [[INSPIRE](#)].
- [11] K.M. Zurek, *Multi-Component Dark Matter*, *Phys. Rev. D* **79** (2009) 115002 [[arXiv:0811.4429](#)] [[INSPIRE](#)].
- [12] S. Baek, P. Ko and W.-I. Park, *Search for the Higgs portal to a singlet fermionic dark matter at the LHC*, *JHEP* **02** (2012) 047 [[arXiv:1112.1847](#)] [[INSPIRE](#)].
- [13] L. Lopez-Honorez, T. Schwetz and J. Zupan, *Higgs portal, fermionic dark matter, and a Standard Model like Higgs at 125 GeV*, *Phys. Lett. B* **716** (2012) 179 [[arXiv:1203.2064](#)] [[INSPIRE](#)].
- [14] M. Heikinheimo, A. Racioppi, M. Raidal, C. Spethmann and K. Tuominen, *Dark Supersymmetry*, *Nucl. Phys. B* **876** (2013) 201 [[arXiv:1305.4182](#)] [[INSPIRE](#)].
- [15] K. Ghorbani, *Fermionic dark matter with pseudo-scalar Yukawa interaction*, *JCAP* **01** (2015) 015 [[arXiv:1408.4929](#)] [[INSPIRE](#)].
- [16] Y.G. Kim, K.Y. Lee, C.B. Park and S. Shin, *Secluded singlet fermionic dark matter driven by the Fermi gamma-ray excess*, *Phys. Rev. D* **93** (2016) 075023 [[arXiv:1601.05089](#)] [[INSPIRE](#)].
- [17] S. Bhattacharya, A. Drozd, B. Grzadkowski and J. Wudka, *Two-Component Dark Matter*, *JHEP* **10** (2013) 158 [[arXiv:1309.2986](#)] [[INSPIRE](#)].
- [18] S. Esch, M. Klasen and C.E. Yaguna, *Detection prospects of singlet fermionic dark matter*, *Phys. Rev. D* **88** (2013) 075017 [[arXiv:1308.0951](#)] [[INSPIRE](#)].

- [19] S. Esch, M. Klasen and C.E. Yaguna, *A minimal model for two-component dark matter*, *JHEP* **09** (2014) 108 [[arXiv:1406.0617](#)] [[INSPIRE](#)].
- [20] S. Ipek, D. McKeen and A.E. Nelson, *A Renormalizable Model for the Galactic Center Gamma Ray Excess from Dark Matter Annihilation*, *Phys. Rev. D* **90** (2014) 055021 [[arXiv:1404.3716](#)] [[INSPIRE](#)].
- [21] Y. Cai and A.P. Spray, *Fermionic Semi-Annihilating Dark Matter*, *JHEP* **01** (2016) 087 [[arXiv:1509.08481](#)] [[INSPIRE](#)].
- [22] J. König, A. Merle and M. Totzauer, *keV Sterile Neutrino Dark Matter from Singlet Scalar Decays: The Most General Case*, *JCAP* **11** (2016) 038 [[arXiv:1609.01289](#)] [[INSPIRE](#)].
- [23] A. Ahmed, M. Duch, B. Grzadkowski and M. Iglicki, *Multi-Component Dark Matter: the vector and fermion case*, *Eur. Phys. J. C* **78** (2018) 905 [[arXiv:1710.01853](#)] [[INSPIRE](#)].
- [24] F. Kahlhoefer, K. Schmidt-Hoberg and S. Wild, *Dark matter self-interactions from a general spin-0 mediator*, *JCAP* **08** (2017) 003 [[arXiv:1704.02149](#)] [[INSPIRE](#)].
- [25] S. Baek, P. Ko and J. Li, *Minimal renormalizable simplified dark matter model with a pseudoscalar mediator*, *Phys. Rev. D* **95** (2017) 075011 [[arXiv:1701.04131](#)] [[INSPIRE](#)].
- [26] G. Arcadi, M. Lindner, F.S. Queiroz, W. Rodejohann and S. Vogl, *Pseudoscalar Mediators: A WIMP model at the Neutrino Floor*, *JCAP* **03** (2018) 042 [[arXiv:1711.02110](#)] [[INSPIRE](#)].
- [27] K. Ghorbani and P.H. Ghorbani, *Leading Loop Effects in Pseudoscalar-Higgs Portal Dark Matter*, *JHEP* **05** (2019) 096 [[arXiv:1812.04092](#)] [[INSPIRE](#)].
- [28] S. Bhattacharya, P. Ghosh and N. Sahu, *Multipartite Dark Matter with Scalars, Fermions and signatures at LHC*, *JHEP* **02** (2019) 059 [[arXiv:1809.07474](#)] [[INSPIRE](#)].
- [29] M. Duch, B. Grzadkowski and D. Huang, *Strong Dark Matter Self-Interaction from a Stable Scalar Mediator*, *JHEP* **03** (2020) 096 [[arXiv:1910.01238](#)] [[INSPIRE](#)].
- [30] M. Cirelli, N. Fornengo and A. Strumia, *Minimal dark matter*, *Nucl. Phys. B* **753** (2006) 178 [[hep-ph/0512090](#)] [[INSPIRE](#)].
- [31] D.G.E. Walker, *Dark Matter Stabilization Symmetries from Spontaneous Symmetry Breaking*, [arXiv:0907.3146](#) [[INSPIRE](#)].
- [32] N. Bernal, D. Restrepo, C. Yaguna and O. Zapata, *Two-component dark matter and a massless neutrino in a new $B - L$ model*, *Phys. Rev. D* **99** (2019) 015038 [[arXiv:1808.03352](#)] [[INSPIRE](#)].
- [33] B.D. Sáez, F. Rojas-Abatte and A.R. Zerwekh, *Dark Matter from a Vector Field in the Fundamental Representation of $SU(2)_L$* , *Phys. Rev. D* **99** (2019) 075026 [[arXiv:1810.06375](#)] [[INSPIRE](#)].
- [34] A. Belyaev, G. Cacciapaglia, J. McKay, D. Marin and A.R. Zerwekh, *Minimal Spin-one Isotriplet Dark Matter*, *Phys. Rev. D* **99** (2019) 115003 [[arXiv:1808.10464](#)] [[INSPIRE](#)].
- [35] O. Catà and A. Ibarra, *Dark Matter Stability without New Symmetries*, *Phys. Rev. D* **90** (2014) 063509 [[arXiv:1404.0432](#)] [[INSPIRE](#)].
- [36] G. Bélanger and J.-C. Park, *Assisted freeze-out*, *JCAP* **03** (2012) 038 [[arXiv:1112.4491](#)] [[INSPIRE](#)].
- [37] F. D’Eramo and J. Thaler, *Semi-annihilation of Dark Matter*, *JHEP* **06** (2010) 109 [[arXiv:1003.5912](#)] [[INSPIRE](#)].

- [38] G. Bélanger, K. Kannike, A. Pukhov and M. Raidal, *Impact of semi-annihilations on dark matter phenomenology – an example of Z_N symmetric scalar dark matter*, *JCAP* **04** (2012) 010 [[arXiv:1202.2962](#)] [[INSPIRE](#)].
- [39] Y. Nomura and J. Thaler, *Dark Matter through the Axion Portal*, *Phys. Rev. D* **79** (2009) 075008 [[arXiv:0810.5397](#)] [[INSPIRE](#)].
- [40] A. Ibarra, A.S. Lamperstorfer, S. López-Gehler, M. Pato and G. Bertone, *On the sensitivity of CTA to gamma-ray boxes from multi-TeV dark matter*, *JCAP* **09** (2015) 048 [Erratum *ibid.* **06** (2016) E02] [[arXiv:1503.06797](#)] [[INSPIRE](#)].
- [41] A. Merle, A. Schneider and M. Totzauer, *Dodelson-Widrow Production of Sterile Neutrino Dark Matter with Non-Trivial Initial Abundance*, *JCAP* **04** (2016) 003 [[arXiv:1512.05369](#)] [[INSPIRE](#)].
- [42] M. Heikinheimo, T. Tenkanen, K. Tuominen and V. Vaskonen, *Observational Constraints on Decoupled Hidden Sectors*, *Phys. Rev. D* **94** (2016) 063506 [Erratum *ibid.* **96** (2017) 109902] [[arXiv:1604.02401](#)] [[INSPIRE](#)].
- [43] Y. Mambrini, S. Profumo and F.S. Queiroz, *Dark Matter and Global Symmetries*, *Phys. Lett. B* **760** (2016) 807 [[arXiv:1508.06635](#)] [[INSPIRE](#)].
- [44] H.M. Lee, M. Park and V. Sanz, *Interplay between Fermi gamma-ray lines and collider searches*, *JHEP* **03** (2013) 052 [[arXiv:1212.5647](#)] [[INSPIRE](#)].
- [45] R.N. Lerner and J. McDonald, *Gauge singlet scalar as inflaton and thermal relic dark matter*, *Phys. Rev. D* **80** (2009) 123507 [[arXiv:0909.0520](#)] [[INSPIRE](#)].
- [46] G. Cynolter, E. Lendvai and G. Pocsik, *Note on unitarity constraints in a model for a singlet scalar dark matter candidate*, *Acta Phys. Polon. B* **36** (2005) 827 [[hep-ph/0410102](#)] [[INSPIRE](#)].
- [47] K. Kainulainen, S. Nurmi, T. Tenkanen, K. Tuominen and V. Vaskonen, *Isocurvature Constraints on Portal Couplings*, *JCAP* **06** (2016) 022 [[arXiv:1601.07733](#)] [[INSPIRE](#)].
- [48] M. Blennow, E. Fernandez-Martinez and B. Zaldivar, *Freeze-in through portals*, *JCAP* **01** (2014) 003 [[arXiv:1309.7348](#)] [[INSPIRE](#)].
- [49] G. Bélanger et al., *LHC-friendly minimal freeze-in models*, *JHEP* **02** (2019) 186 [[arXiv:1811.05478](#)] [[INSPIRE](#)].
- [50] T. Bringmann, P.F. Depta, M. Hufnagel, J.T. Ruderman and K. Schmidt-Hoberg, *Pandemic Dark Matter*, [arXiv:2103.16572](#) [[INSPIRE](#)].
- [51] A. Hryczuk and M. Laletin, *Dark matter freeze-in from semi-production*, *JHEP* **06** (2021) 026 [[arXiv:2104.05684](#)] [[INSPIRE](#)].
- [52] G. Bélanger, F. Boudjema, A. Pukhov and A. Semenov, *MicrOMEGAs4.1: two dark matter candidates*, *Comput. Phys. Commun.* **192** (2015) 322 [[arXiv:1407.6129](#)] [[INSPIRE](#)].
- [53] L. Husdal, *On Effective Degrees of Freedom in the Early Universe*, *Galaxies* **4** (2016) 78 [[arXiv:1609.04979](#)] [[INSPIRE](#)].
- [54] G. Bélanger, A. Pukhov, C.E. Yaguna and O. Zapata, *The Z_5 model of two-component dark matter*, *JHEP* **09** (2020) 030 [[arXiv:2006.14922](#)] [[INSPIRE](#)].
- [55] T.N. Maity and T.S. Ray, *Exchange driven freeze out of dark matter*, *Phys. Rev. D* **101** (2020) 103013 [[arXiv:1908.10343](#)] [[INSPIRE](#)].

- [56] B. Díaz Sáez, K. Möhling and D. Stöckinger, *Two Real Scalar WIMP Model in the Assisted Freeze-Out Scenario*, *JCAP* **10** (2021) 027 [[arXiv:2103.17064](#)] [[INSPIRE](#)].
- [57] CMS collaboration, *Search for invisible decays of a Higgs boson produced through vector boson fusion in proton-proton collisions at $\sqrt{s} = 13$ TeV*, *Phys. Lett. B* **793** (2019) 520 [[arXiv:1809.05937](#)] [[INSPIRE](#)].
- [58] PLANCK collaboration, *Planck 2018 results. VI. Cosmological parameters*, *Astron. Astrophys.* **641** (2020) A6 [Erratum *ibid.* **652** (2021) C4] [[arXiv:1807.06209](#)] [[INSPIRE](#)].
- [59] XENON collaboration, *Dark Matter Search Results from a One Ton-Year Exposure of XENON1T*, *Phys. Rev. Lett.* **121** (2018) 111302 [[arXiv:1805.12562](#)] [[INSPIRE](#)].
- [60] XENON collaboration, *Physics reach of the XENON1T dark matter experiment*, *JCAP* **04** (2016) 027 [[arXiv:1512.07501](#)] [[INSPIRE](#)].
- [61] T. Binder, T. Bringmann, M. Gustafsson and A. Hryczuk, *Early kinetic decoupling of dark matter: when the standard way of calculating the thermal relic density fails*, *Phys. Rev. D* **96** (2017) 115010 [Erratum *ibid.* **101** (2020) 099901] [[arXiv:1706.07433](#)] [[INSPIRE](#)].
- [62] S.S. AbdusSalam et al., *Simple and statistically sound strategies for analysing physical theories*, [arXiv:2012.09874](#) [[INSPIRE](#)].
- [63] A. Ibarra, S. López Gehler and M. Pato, *Dark matter constraints from box-shaped gamma-ray features*, *JCAP* **07** (2012) 043 [[arXiv:1205.0007](#)] [[INSPIRE](#)].
- [64] G. Vertongen and C. Weniger, *Hunting Dark Matter Gamma-Ray Lines with the Fermi LAT*, *JCAP* **05** (2011) 027 [[arXiv:1101.2610](#)] [[INSPIRE](#)].
- [65] A. Ghosh, A. Ibarra, T. Mondal and B. Mukhopadhyaya, *Gamma-ray signals from multicomponent scalar dark matter decays*, *JCAP* **01** (2020) 011 [[arXiv:1909.13292](#)] [[INSPIRE](#)].
- [66] F.S. Queiroz and C. Siqueira, *Search for Semi-Annihilating Dark Matter with Fermi-LAT, H.E.S.S., Planck, and the Cherenkov Telescope Array*, *JCAP* **04** (2019) 048 [[arXiv:1901.10494](#)] [[INSPIRE](#)].
- [67] A. Reinert and M.W. Winkler, *A Precision Search for WIMPs with Charged Cosmic Rays*, *JCAP* **01** (2018) 055 [[arXiv:1712.00002](#)] [[INSPIRE](#)].